

# Dynamic coupling of a finite element solver to large-scale atomistic simulations

Mihkel Veske<sup>1</sup>, Andreas Kyritsakis<sup>1</sup>, Kristjan Eimre<sup>2</sup>, Vahur Zadin<sup>2</sup>, Alvo Aabloo<sup>2</sup> and Flyura Djurabekova<sup>1</sup>

<sup>1</sup>Department of Physics and Helsinki Institute of Physics, University of Helsinki, PO Box 43 (Pietari Kalmin katu 2), 00014 Helsinki, Finland

<sup>2</sup>Intelligent Materials and Systems Lab, Institute of Technology, University of Tartu, Nooruse 1, 50411 Tartu, Estonia

E-mail: mihkel.veske@helsinki.fi

## Abstract

We propose a method for efficiently coupling the finite element method with atomistic simulations, while using molecular dynamics or kinetic Monte Carlo techniques. Our method can dynamically build an optimized unstructured mesh that follows the geometry defined by atomistic data. On this mesh, different multiphysics problems can be solved to obtain distributions of physical quantities of interest, which can be fed back to the atomistic system. The simulation flow is optimized to maximize computational efficiency while maintaining good accuracy. This is achieved by providing the modules for a) optimization of the density of the generated mesh according to requirements of a specific geometry and b) efficient extension of the finite element domain without a need to extend the atomistic one. Our method is organized as an open-source C++ code. In the current implementation, an efficient Laplace equation solver for calculation of electric field distribution near rough atomistic surface demonstrates the capability of the suggested approach.

Keywords: multiphysics, multiscale, electric field, Laplace equation, finite element method, atomistic simulation

## 1. Introduction

Achieving atomistic spatial and temporal resolution is still challenging for experimental physics and, in many cases, numerical simulations based on well-motivated physical models are the only tools which can provide interesting insight on the atomic scale. However, due to an unavoidable trade-off between computational efficiency and desired accuracy, often seemingly promising computational models turn out to be impractical.

One way to achieve high computational efficiency and numerical accuracy is to combine continuous-space calculations with atomistic simulations like classical molecular dynamics (MD) or kinetic Monte Carlo (KMC). Some such approaches [1]–[4] have shown promising results when simulating the elastoplastic evolution of nanostructures. Others [5]–[9], being especially relevant to the present work, have used such a technique to study the effects of electric field around nanostructured materials.

When a strong electric field is applied on the surface of a metal, it induces surface charge and polarization, and under certain circumstances, it triggers field emission currents with consequent electromigration effects [10]. Thus, the high electric field may significantly affect the evolution of the system and under certain conditions might cause major surface deformations [11]. For that reason, atomistic simulations that take into account the effects of electrostatic field have a wide range of applications in atom probe tomography (APT) [12], nanoelectronics [13] and space technology [14]. Moreover, atomistic modeling is a valuable tool in investigation of vacuum arcing phenomena (vacuum breakdowns), as the fundamental mechanisms that trigger a breakdown are not entirely clear yet. The breakdown studies are relevant to the development of new-generation linear colliders like CLIC in CERN [15], vacuum interrupters [16], free electron lasers [17] and fusion devices [18].

Simulating electronic processes on material surfaces requires an accurately calculated spatial distribution of the electric field. The common method for calculating the field around any geometry is to build a mesh around the system of interest and solve the Laplace or Poisson equation on it. The solver is usually based on the finite difference method (FDM) [9], [19], finite element method (FEM) [7] or their modifications [6]. Many authors [8], [20] calculate the electric field around nanostructures without building any mesh around it. Although such mesh-free methods might be more flexible and efficient under certain conditions, they are limited in practical applications as they incorporate only the calculation of electric field.

The mesh for solving the differential equations can be either static (it does not change during the evolution of the underlying atomistic geometry) or dynamic (the mesh is adjusted with the movement of the atoms). Both can be either structured or unstructured. The main advantage of a structured mesh is its implementation simplicity, while the unstructured one provides higher tolerance to the underlying geometry. Although the generation of an unstructured dynamic mesh requires significant computational effort, it has considerable advantages over the alternatives. Since it is reconstructed at every simulation step, its shape will accurately follow the underlying geometry with the optimal density in each region. This ensures high robustness against changes in the crystallographic structure of the material, good scalability and maximum accuracy for a given computational cost.

Effects of electric field, thus far, have been introduced in atomistic simulations based on a structured or unstructured static mesh approaches. The mesh that is generated in those works either lacks accuracy in following the underlying geometry [7] or is unnecessarily dense [6], making the total

computational cost unfeasible to be performed iteratively. Also, previous works are rather not universal as they typically focus on a specific type of differential equations.

The present work is the continuation of our previous attempt to include the electronic effects in atomistic simulations by solving the Laplace equation in a structured static mesh using FDM [5]. The method enabled us to investigate the behavior of Cu surface under high electric field when small-scale surface features are present [21]–[26]. However, the high computational cost and inflexible mesh limited the earlier simulations to a specific crystal structures and orientations, few nm scale and very short times. To cope with the forthcoming challenges of large scale dynamic simulations, we generalized the method by combining the dynamic mesh approach with the FEM [27]. In this way, we provide a framework for solving multiple differential equations in the vacuum and material domains, in order to achieve enhanced computational efficiency, scalability and tolerance with respect to the crystallographic structure of studied materials. The framework also allows us to use the results in iterative atomistic simulations like MD and KMC.

## 2. Methodology

### 2.1. Overview

The main objective of the current project is to provide a tool for calculating the effects of electric field on atomistic systems for up to  $10^7$  atoms with a reasonable computational effort. For that purpose, we provide an open-source C++ code that contains the modules which enable to:

- import atomistic coordinates of a nanostructure from the atomistic simulation;
- dynamically generate an unstructured mesh around the imported structure;
- solve the differential equations of interest on the mesh;
- return the solution to the atomistic simulation.

By using FEM for solving the differential equations, we are able to optimize the mesh density in various parts of the simulation domain. In regions of high interest, where the solution changes rapidly, the mesh can be made denser and in regions with small solution gradient and lower interest the mesh could be coarser. However, generating a mesh with an appropriate density is rather obligatory as performing the calculation in a poorly optimized mesh is impractical in terms of computational cost. In our simulations, we are mostly interested in the processes that take place on the surface of the material. For that reason, the mesh we generate to follow the surface geometry is dense near the surface, becoming gradually coarser away from it. However, to meet the needs of a wider audience, such an optimization scheme can be easily overridden by the user.

In the following paragraphs we describe the methodology to perform the tasks listed above. Appendix A summarizes the different simulation stages with a flowchart.

## 2.2. Surface extraction

We classify the atoms of the whole material as surface, bulk and clustered or evaporated atoms. The latter ones are often present in high electric field simulations, where detachment of a part of the nanotip may happen due to field-assisted evaporation [28]. To handle such systems, we perform cluster analysis on the input atoms and separate the clustered and evaporated atoms from the rest of the material. This analysis is done by using the DBSCAN (Density-Based Spatial Clustering of Applications with Noise) algorithm [29], which allows for efficient grouping of closely packed atoms without imposing any restrictions to the system geometry.

To distinguish the surface atoms from the bulk, we use a two-step procedure. In the first step, we use a computationally efficient coordination analysis – atoms with low coordination (small number of nearest neighbors (NN)) are classified as possible surface atoms, while highly coordinated atoms are recognized as bulk. In the second step, we build a Voronoi tessellation around the atoms with low coordination number. Atoms whose Voronoi cell has at least one facet exposed to the vacuum are considered to reside on the surface, while the others are located in the bulk (see figure 1). The evaporated atoms, for which all the Voronoi facets would be exposed to the vacuum, have already been identified by the cluster analysis.

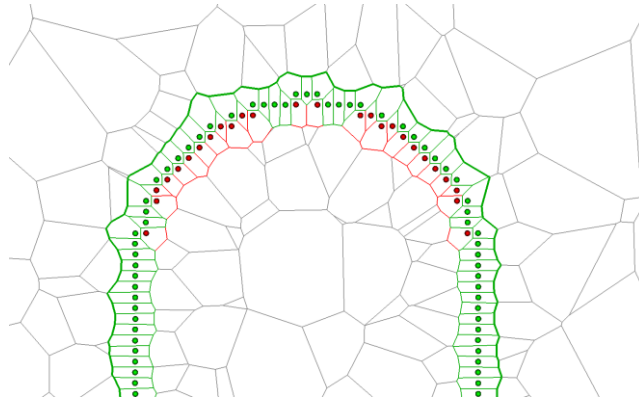


Figure 1. Slice of the Voronoi cells generated around the atoms with low coordination. The cell facets can be used to separate the surface atoms (green) from the bulk (red).

It is important to mention that such a two-step extraction is needed only in systems where the atoms are not strictly bound to the rigid crystal lattice. If the atoms do not move far away from their sites in a regular lattice, the surface extraction by the coordination analysis is sufficient and the computationally less efficient Voronoi cleaner can be skipped.

## 2.3. Surface coarsening and smoothing

In general, there are two ways to generate a coarsened mesh – the top-down and the bottom-up methods. In the top-down technique, a dense mesh is generated first and then specific algorithms are used to decrease the density of elements in regions of low interest. Such an approach is useful when most of the resulting mesh is supposed to be dense and the coarsening needs to be done in a small region. The bottom-up approach, however, starts with a coarse mesh and gradually refines it until the

desired quality criteria are met. The latter method turns out to be more effective if – as in our case – most of the resulting mesh is supposed to be coarse.

The total mesh generation time can be significantly reduced by making the initial, not yet refined, mesh as close as possible to the desired final one. To achieve this, it is necessary to use appropriate mesh generators, i.e. points that follow the material surface and the simulation domain boundaries and will be nodes of the initial mesh. The generators can be obtained by designing a function which selects them among the surface atoms. Such a function has to ensure that the resulting generators have the desired density in different material regions. Therefore, for every surface atom with coordinates  $\mathbf{r}$ , the function should determine a clearance radius  $R_{cut}$  that can be used to remove neighboring atoms which are too close (see figure 2). For instance, in systems where a cylindrical nanotip is covered with a hemisphere, we have obtained good results by using a formula as follows:

$$R_{cut}(\mathbf{r}) = \begin{cases} c_1\lambda/4, & |\mathbf{r} - \mathbf{r}_{apex}| \leq R, & \text{I} \\ c_2\lambda/4, & |\mathbf{r} - \mathbf{r}_{apex}| > R \wedge |\mathbf{r} - \mathbf{r}_0|_{x,y} \leq R, & \text{II} \\ c_3 0.1\lambda\sqrt{|\mathbf{r} - \mathbf{r}_0| - R} + c_2\lambda/4 & \text{otherwise,} & \text{III} \end{cases} \quad (1)$$

where  $R$  is the radius of the cylinder and hemisphere,  $\mathbf{r}_{apex}$  is the center of the nanotip apex,  $\mathbf{r}_0$  is the center of the nanotip-substrate junction and  $\lambda$  is a characteristic distance between NN atoms. In crystalline systems  $\lambda$  can be equalized to the crystal lattice constant. Parameters  $c_1$ ,  $c_2$  and  $c_3$  are the integer coarsening factors that define the density of the mesh around the nanotip apex (region I in equation (1) and figure 2), nanotip lateral facets (region II) and substrate surface (region III), respectively. In general, it is necessary to specify a unique set of  $c_i$  factors for each simulation geometry to meet the compromise between computational cost and solution accuracy.

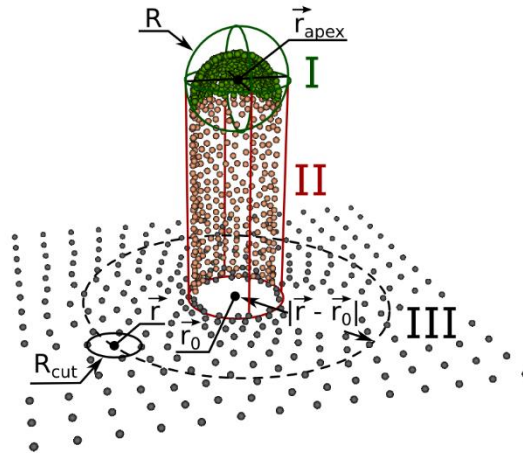


Figure 2. Principle for coarsening the nanotip surface.  $R_{cut}$  – clearance radius around an atom in a position  $\mathbf{r}$ ,  $R$  – radius of the cylinder and hemisphere,  $\mathbf{r}_{apex}$  – center of the nanotip apex,  $\mathbf{r}_0$  – center of the nanotip-substrate junction. The coloring of the nodes along with the Roman numerals designate the coarsening regions in equation (1).

It is important to mention that this coarsening scheme can be used not only for the single nanotips, but for any geometry where the region of interest fits into a single cylinder. Geometries with several regions of interest that are separated by areas of low priority demand a customized approach.

After the surface coarsening, we apply weighted Laplace averaging for the points inside the cylinder to make the resulting mesh smoother. As a result of the smoothing, the coordinates of the  $i$ -th point will be the weighted average of the coordinates of its neighboring points, i.e.

$$\mathbf{r}_i = \frac{\sum_{j \neq i} w_{ij} \mathbf{r}_j}{\sum_{j \neq i} w_{ij}}, \quad w_{ij} = \exp\left(-\frac{|\mathbf{r}_i - \mathbf{r}_j|}{\lambda\beta}\right), \quad (2)$$

where  $w_{ij}$  is the statistical weight of the  $j$ -th neighboring point. The smoothing factor  $\beta$  allows to control the sharpness of the smoothing – the higher the value the stronger the averaging. In our simulations we use small smoothing values (typically  $\leq 0.1$ ). This guarantees smoother surface mesh while keeping the geometric distortions small.

#### 2.4. Mesh generation

After defining the surface atoms and the size of the simulation box, we perform a Delaunay triangulation based mesh generation in a 3D space by using the open-source software package Tetgen [30]. As a result, we create tetrahedra that fill the simulation domain and pass through the generators. The next step is to check for the quality (minimum edge – outer radius ratio) and maximum volume of the resulting tetrahedra. The mesh is refined iteratively until all tetrahedra meet the specified quality and volume criteria, and the result can be used as a finite element mesh. The details about Delaunay tetrahedralization can be found elsewhere [6], [27], [30].

To increase the computational efficiency of the FEM solver and obtain higher spatial resolution for the solution, we divide each tetrahedron into four hexahedra. For this we append an additional node in the centroid of each tetrahedron, triangle and line in the mesh (see the inset of figure 3).

#### 2.5. Calculation of the electric field

The generated mesh is used to solve the differential equations of interest. In the current implementation we only solve the Laplace equation (for maximum computational efficiency we assume a negligible charge density in the vacuum) to find the electrostatic potential  $\Phi(\mathbf{r})$  distribution around the nanostructure:

$$\Delta\Phi = 0. \quad (3)$$

The electric field is obtained by calculating the gradient of the electrostatic potential:

$$\mathbf{E} = -\nabla\Phi. \quad (4)$$

Since we are mainly simulating metals, we apply the Dirichlet boundary condition (BC) on the surface to obtain there a constant potential:

$$\Phi|_{surface} = 0. \quad (5)$$

A Neumann BC on top of the simulation box ensures that the long-range electric field is uniform:

$$-\nabla\Phi|_{top} = \mathbf{E}_0. \quad (6)$$

Furthermore, in order to apply periodic BC on the lateral directions, we assume zero electric flux between the mirror images of the system, i.e

$$(\mathbf{n} \cdot \nabla\Phi)|_{perimeter} = 0, \quad (7)$$

where  $\mathbf{n}$  is the surface normal vector. Finally, once the mesh is generated and the BCs have been set, the Laplace equation is solved using the open-source library Deal.II [31].

### 2.6. Local solution extraction

Once the boundary condition problem has been solved, the solution has to be extracted at points of interest that may or may not lie inside the mesh. The FEM solver can export the solution at any internal point of the mesh, however point-by-point extraction costs significant computational time and does not allow extrapolation slightly off the mesh. A workaround to this issue is to first extract the solution at all the tetrahedral nodes (it has a very efficient implementation in the solver) and then interpolate (or extrapolate) it by using linear tetrahedral interpolation (LTI) [32]. This way we significantly reduce the total interpolation time as for each tetrahedron there are four hexahedra in the mesh. At the same time we do not lose much in accuracy as the characteristic edge length in the apex region is half of the distance between the NN atoms.

The strategy of LTI is to calculate the barycentric coordinates [33] for the point of interest and use them to find the tetrahedron that surrounds it. Denoting by  $m_{ijk}$  the  $k$ -th barycentric coordinate of a point  $i$  with respect to a tetrahedron  $j$ , the point is surrounded by the tetrahedron if and only if

$$m_{ijk} \geq 0 \quad \forall k = 1,2,3,4. \quad (8)$$

Knowing the solution  $\Psi_{jk}$  ( $\Psi$  can be any calculated quantity, e.g electric field or potential) on the node  $k$  of the tetrahedron  $j$ , the barycentric coordinates can be used as weights for the interpolation [33]. Thus the solution at the point of interest  $i$  that is surrounded by that tetrahedron will be

$$\Psi_i = \sum_k m_{ijk} \Psi_{jk}, \text{ with } \sum_k m_{ijk} = 1. \quad (9)$$

Note that normalization is an inherent property of the barycentric coordinates.

A significant part of the computational cost of such an interpolation method consists of finding the tetrahedron that surrounds the interpolation point or locating the one which is nearest to it. The cost can be reduced by increasing the data locality, i.e by sorting the interpolation points in a way that every next point is located close to the previous one. This way every subsequent point is located in the same tetrahedron as the previous one or inside one of its neighboring tetrahedra. We achieve such a spatial ordering by sorting the points of interest along a 3D Hilbert curve [34].

### 2.7. Smoothing the results

An inherent feature of the FEM is its strong dependence on the quality of the mesh. The higher the symmetry of the elements and the smoother the mesh, the more accurate results can be obtained. In continuous geometries, there is no theoretical limit to refining the mesh – and thus improving the solution accuracy – while following the underlying geometry. In atomistic simulations, however, the physical limit of the accuracy is drawn by the discreteness of the atomistic system. As the surface is inherently rough on an atomic scale, the same roughness will present itself in the mesh generated on top of it. It is possible to apply various surface smoothing algorithms like Laplace averaging, spline interpolation etc., but all of them distort the geometry, affect the accuracy of the solution and increase significantly total computation time. Nevertheless, a mesh with asperities at the surface may lead to artificially enhanced electric fields on some surface nodes.

To remove such “spikes” in the electric field distribution, we developed an algorithm to smoothen the electric field. The algorithm takes advantage of the fact that the largest asperities with potentially the most inaccurate solution are always located in the nodes of the tetrahedra. The rest of the nodes are on the centroids of the tetrahedra, triangles or lines and are therefore always guaranteed to have flat neighborhood at least in 1 dimension. Thus the algorithm replaces the electric field in the tetrahedral nodes with the weighted average field on its surrounding hexahedral nodes (see figure 3). After the averaging, the electric field in the  $i$ -th tetrahedral node will be

$$\mathbf{E}_i = \frac{\sum_{j \neq i} w_{ij} \mathbf{E}_j}{\sum_{j \neq i} w_{ij}}, \quad w_{ij} = e^{-|r_i - r_j|}, \quad (10)$$

where  $\mathbf{E}_j$  is the electric field in the  $j$ -th node of all the hexahedra that contain the  $i$ -th node and  $w_{ij}$  is the statistical weight that is a function of a distance between a tetrahedral and a hexahedral node. The sample comparison of the results with and without the post-processing is shown in figure 4.

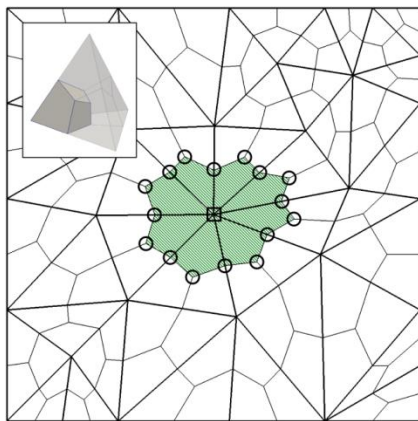


Figure 3. 2D illustration of averaging of the electric field in the nodes of the tetrahedra. Circles show the nodes of the hexahedra that contribute to the weighted average solution in the node of a tetrahedron, which is marked by a square. Inset: the division of a tetrahedron into four hexahedra.

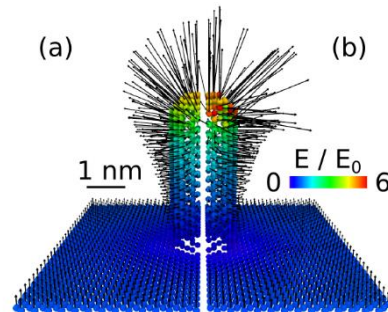


Figure 4. Electric field distribution around a cylindrically symmetric nanotip with (a) and without (b) the post-processing. The arrows indicate the magnitude and direction of the local electric field. The color coding represents the local field enhancement factor.



## 2.8. *Special optimization features*

Our code is designed to be combined with atomistic simulations, such as MD or KMC. To increase the overall efficiency, several features were added to the code to reduce the CPU and memory consumption of the multiscale simulations.

### 2.8.1. *Extending the simulation domain*

In atomistic simulations, the phenomena of interest are often well localized in a certain region, while the rest of the simulation domain is present to eliminate undesired effects appearing due to the periodic boundary conditions. Many such effects can be reduced by increasing the size of the simulation domain. Increasing the system size by adding extra atoms requires a significant increase of computational resources.

The usage of the FEM, however, allows building an extended simulation domain more efficiently. As the current approach was developed for simulating the processes on or near the surfaces, we extend the system by extending the surface, as demonstrated in figure 5. The shape of the extended surface can be defined either by providing an analytical formula that describes it, or by directly inputting the location of the additional nodes from a pre-built file.

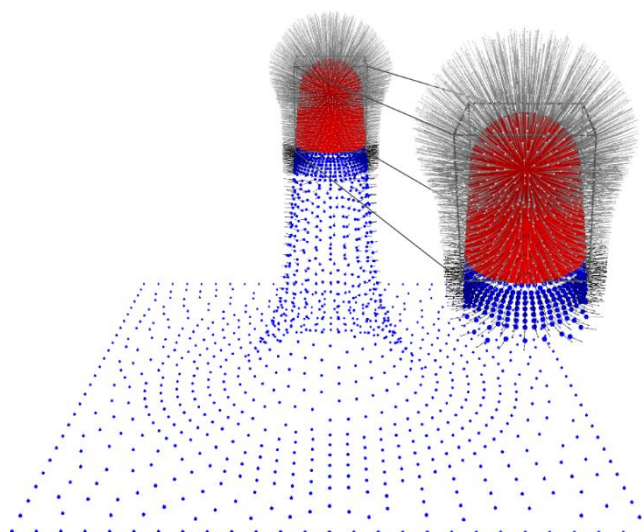


Figure 5. Extending the surface around the atomistic data. Red points inside the box – nodes from the atomistic simulation; blue points outside the box – nodes of the extended surface. Arrows around the nanotip indicate the magnitude and direction of local electric field. The arrows have different colors in MD and extended region for visual purposes.

### 2.8.2. *Reusing the solution*

Typically atoms move within a few percent of an angstrom during one MD timestep. As the expected change in the system geometry is rather small, it is reasonable to expect that due to the stability of the Laplace equation [35], the change in the solution will be insignificant. Taking into account that due to numerical errors the calculated electric field always fluctuates, it appears that the field might be reused in several MD iterations, if the change in the system geometry is non-significant.

To use such an approximation in practice, we estimate the change in the system geometry by calculating the root mean square (rms) distance the atoms have moved since the last full iteration. The advantage of the rms value over the average is its higher sensitivity on major local geometry changes, as the longer distances have greater rank than shorter ones. We vary the tolerance of the optimizer by changing the pre-specified threshold the atoms should move in order to fully recalculate the field.

### 3. Results

The described algorithms are organized as an open-source software package called FEMOCS that can be freely downloaded from [36]. The proposed code can be used either as a standalone application or as a library. For the latter case we implemented C, C++ and Fortran interfaces that enable the usage of FEMOCS with only minor modifications in the main code. In the standalone mode, the code can read atomistic coordinates from a file and run the mesh generator and differential equation solver for these data. There is also an option to omit the atomistic section, import the mesh from a file and solve the differential equations on it.

In the following sections, we demonstrate the accuracy, speed and robustness of the code by running it on several test cases.

#### 3.1. Validation of the model

We validate our code by calculating the electric field around a hemisphere on a flat planar substrate (figure 6), as this is a geometry for which the Laplace equation has a well-established analytical solution. The appendix B contains more details on the formulas, along with an estimation of the box-size-related systematic errors.

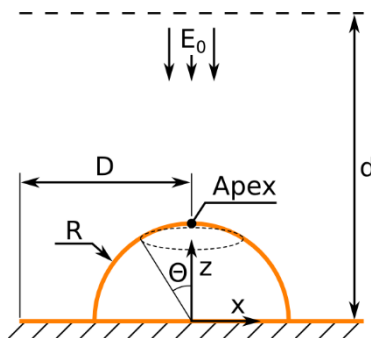


Figure 6. The geometry used to numerically calculate the field distribution. On a rectangular substrate with a thickness of 1nm and a width of  $2D = 10R$ , there is a hemispherical nanotip with radius  $R$  that is exposed to the vacuum and to the electric field. The uniform electric field  $E_0$  is applied as a boundary condition at a distance  $d$  from the surface of the substrate. Polar angle  $\theta$  is used during the error analysis. The system is periodic in lateral directions.

To demonstrate the numerical stability of the code, we first test it on a pseudo-atomistic hemispherical system with high rotational symmetry. We construct the hemisphere by placing the nodes symmetrically to the  $z$ -axis and by ensuring the characteristic distance  $\lambda$  between the NN nodes. This way we can generate a smooth mesh which does not introduce “spikes” into the electric field

distribution. Thus it is possible to estimate the impact of the field post-processor to the solution accuracy and also demonstrate the convergence of the numerical solution to the analytical one.

Furthermore, in order to test the method on a more realistic atomistic system, we replace the symmetric smooth surface with a faceted atomistic one. For this we cut the hemisphere and substrate out from a  $\langle 100 \rangle$  FCC single crystal with a lattice constant of 3.61 angstroms (Cu).

The solution accuracy depends on the mesh density which can be varied by specifying the maximum tetrahedron volume or by altering the coarsening factors of equation (1) as

$$c_1 = c_2 = c_3 = c = 0, 1, 2, \dots \quad (11)$$

For the smooth surface system, the density can also be controlled by varying the  $\lambda$  parameter. Note that the latter scheme cannot be used while coupling the code with atomistic simulations where the characteristic distance between the NN atoms cannot be arbitrarily changed.

### 3.1.1. Solution accuracy in vacuum

The comparison of the analytical solution in space with the one obtained from our code for the atomistic system is shown in figure 7. The graphs show the isolines of the electric field as calculated analytically (a, c) and numerically for two different mesh spatial densities (b, d). As can be seen, the calculated solution progressively deviates from the analytical one with increasing distance from the surface. This error can be reduced by decreasing the maximum allowed volume of the elements. Nevertheless, the solution accuracy on the surface is mainly determined by the size and quality of the mesh in its vicinity. Therefore, although a denser spatial mesh may be required in some of the potential applications of the developed code, it is mostly unnecessary while simulating surface phenomena.

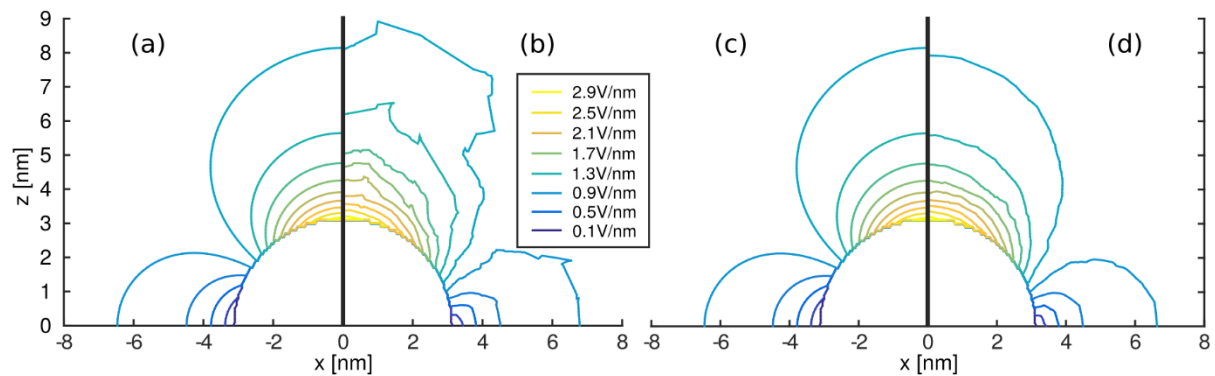


Figure 7. Electric field distribution around a hemisphere with a radius of 3 nm located on a flat surface. (a) & (c) – analytical result, (b) – numerical result in a coarse mesh with maximum element volume  $V_{max} = 5\text{nm}^3$ , (d) – numerical result in a dense mesh with  $V_{max} = 0.05\text{nm}^3$ . In all cases the long-range electric field  $E_0 = 1\text{V/nm}$ .

### 3.1.2. Solution accuracy on smooth surface

In order to demonstrate the solution accuracy near the smooth surface, we denote the magnitudes of numerical and analytical electric fields as  $E$  and  $E_a$ , respectively, and define the field error-value

$$\epsilon = \frac{E - E_a}{E_a}. \quad (12)$$

We use equation (12) to show the solution fluctuation that arises due to the numerical errors in the FEM. For this we measure the error (12) for all the tetrahedral nodes that lie on the hemispherical surface at a polar angle  $\theta$  (a region marked with a dashed line in figure 6). Figure 8 shows the mean value of  $\epsilon$  together with error bars that correspond to its standard error within 95% confidence level. The graph confirms the general trend that coarser mesh results in less accurate field. It also shows that the error does not change significantly along the hemisphere. The same applies to the fluctuation amplitude of the error – in a coarse mesh the error fluctuates up to 3% while in a dense one the fluctuation is less than 1%. Furthermore, the mean error  $\bar{\epsilon}$  is close to the relative distance between the NN nodes. For example, in a dense mesh with  $\lambda/R = 1.7\%$  the numerical field deviates by  $(1 \pm 1)\%$  from the analytical value, while in a coarse mesh with  $\lambda/R = 8.3\%$  that deviation is  $(7 \pm 2)\%$ .

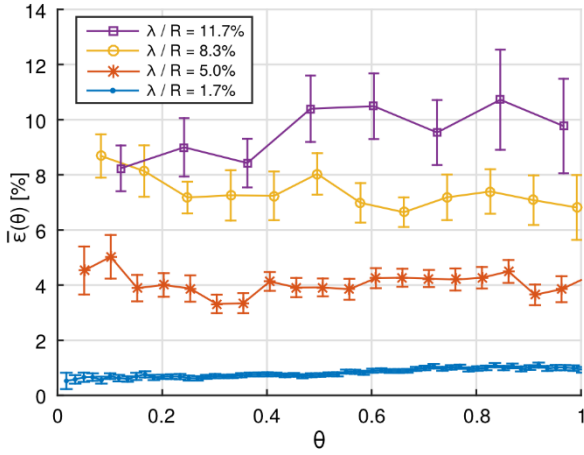


Figure 8. Error of the electric field magnitude along the surface with various mesh densities. Error bars show the standard error of  $\bar{\epsilon}$  value within 95% confidence level.

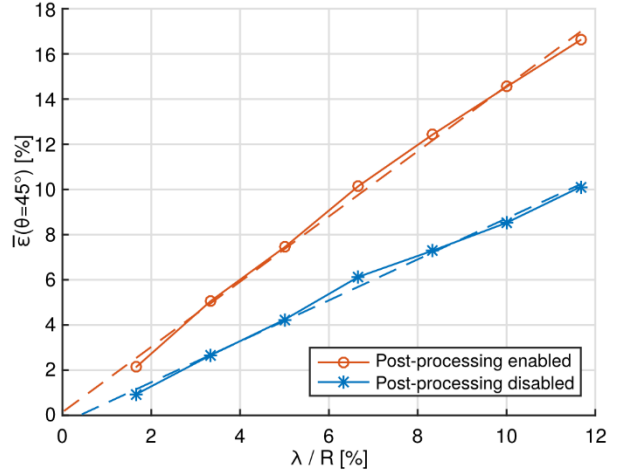


Figure 9. Error of the electric field magnitude near the surface with and without the field post-processor. Solid and dashed lines show the data points and their linear fitting, respectively, and demonstrate the solution convergence.

To show the effect of the field post-processing on the accuracy of the results, we measured the error  $\bar{\epsilon}$  at a fixed polar angle of  $\theta = 45^\circ$ , both with and without the post-processing. Figure 9 demonstrates the results of this measurement. As can be seen, the post-processor tends to decrease the field magnitude. For example, if the characteristic distance between the NN nodes is 10% of the hemisphere radius, the post-processing decreases the field by 6.8% in relation to the unprocessed value. Fitting the dependency (straight dashed line in figure 9) gives a more accurate estimation – the error of field with the post-processor is about 1.6 times higher than without it. This tendency is caused by the smoothing algorithm that replaces the field on the surface with the weighted average fields on and above the surface, where the field has always slightly smaller magnitude. Increasing the mesh density brings the hexahedral nodes closer to the tetrahedral ones and in the limiting case of infinitely dense mesh the numerical solution converges to the analytical one.

### 3.1.3. Solution accuracy on atomistic surface

To show the solution accuracy on the atomistic surface, we calculate the mean error  $\bar{\epsilon}$  for all the tetrahedral nodes that lie on the atomistic hemisphere and inside the cone with semi-vertex angle of  $60^\circ$ . We repeat this measurement for various coarsening factors with and without using the field post-processing. The results are shown in figure 10. The graph confirms again the general trend that coarser mesh results in less accurate field. However, in atomistic systems this trend is not strictly monotonous and its extent depends on the system size. Small systems with a small hemisphere radius tolerate only slight coarsening before the numerical solution quickly deviates from the analytical one. Larger systems, on the other hand, tolerate rather heavy coarsening without losing much of their accuracy.

It is noteworthy that both small and large systems tend to show more accurate results if at least a slight coarsening is applied to the mesh. Moreover, in dense systems with large hemisphere radius the field post-processor significantly increases the solution accuracy, while in small and coarse systems the results are more accurate without the post-processing. This can be explained by the FEM's sensitivity against sharp corners in the mesh – coarsening makes the mesh smoother and reduces the amount of non-physical artifacts in the solution before its post-processing. Therefore we conclude that moderate coarsening of atomistic systems does not only reduce the problem size (thus reducing the computational cost), but also increases the solution accuracy. Moreover, at a given geometry and mesh density, the solution accuracy in large systems always exceeds the accuracy in small ones.

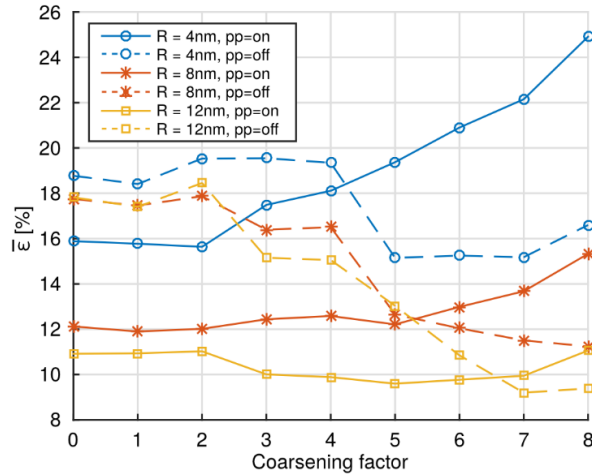


Figure 10. Error of the electric field near the atomistic surface with increasing coarseness and varying hemisphere radius  $R$ . Solid lines show the error if field post-processing is enabled and dashed lines depict the case where it is disabled.

### 3.2. Computational efficiency

For benchmarking purposes we simulated atomistic hemispherical systems as described in section 3.1. We measured the variation of the code execution time for systems with different sizes and different coarsening factors (see figure 11 and figure 12). As all the linear dimensions of the system were chosen to be proportional to the radius  $R$ , the resulting number of atoms in the system scales roughly as  $O(R^3)$ . As can be seen, the computational cost is a sublinear function of the number of atoms in the

system and decreases exponentially with increasing mesh coarsening level. Those results indicate that the computational efficiency (CPU time per atom) of our code increases as the system grows.

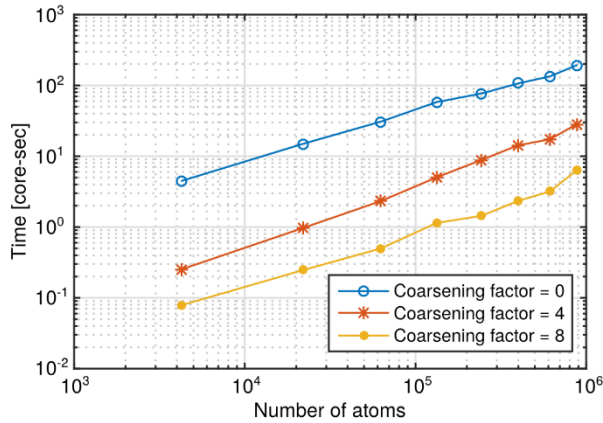


Figure 11. Code execution time dependence on the system size for various mesh coarsening factors.

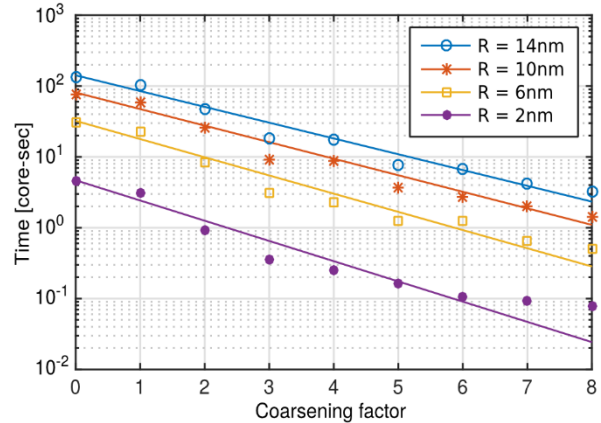


Figure 12. Code execution time dependence on the mesh coarsening factor for systems with different size.

### 3.3. Robustness of the results

To demonstrate the robustness of our algorithms against the crystallographic structure of the material, we calculated the electric field around a nanotip with a molten apex. For this, we placed a cylindrical nanotip with hemispherical cap on the substrate and ran an MD simulation to melt the nanotip apex. The system was cut out from a single-crystalline FCC block with  $\langle 100 \rangle$  orientation and a lattice constant of 3.61 angstroms (Cu). The initial height and diameter of the tip was 24 nm and 6 nm respectively. Inside the tip, we applied a non-uniform ramp temperature distribution along the  $z$  direction with 600 K at the bottom and 1600 K at the top. As the simulation proceeded, the apex of the nanotip melted and formed an atomistic system with mixed amorphous-crystalline structure.

Figure 13 illustrates three different stages of this simulation. Sections (a, b, c) show the evolution of the atomistic system, its local crystal structure as determined by common neighbor analysis [37] and the local electric field on the surface atoms. Sections (d, e, f) demonstrate the corresponding mesh that is generated around the nanotip. It is clearly visible that although a significant part of the nanotip is amorphous and has a transition region between amorphous and crystalline sections, our code manages to calculate a smooth electric field distribution in the whole simulation domain.

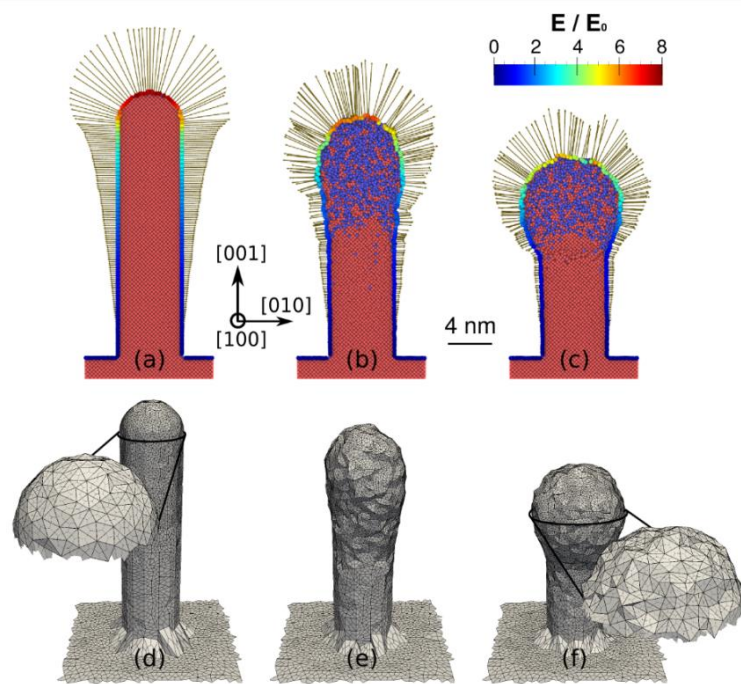


Figure 13. (a)-(c): cross-sections of the nanotip from different stages of the MD simulation. The surface atoms are colored by the local electric field strength, while the color in the atomistic bulk region represents the local crystal structure as determined by common neighbor analysis; red – FCC, blue – amorphous. The arrows around the nanotip indicate the magnitude and direction of the local electric field. (d)-(f): the surface faces of the mesh at the same timesteps.

Finally, we ran a test to verify the robustness and stability of our method against small fluctuations in the input data. We created an FCC  $\langle 100 \rangle$  surface with a single adatom on it. The adatom was placed in  $n = 100$  random lattice positions near the center of the surface and the electric field was calculated for every case. Although the field distribution should not depend on the position of the adatom, it still fluctuates in the FEM calculation due to the rebuilding of the mesh for every iteration. The test showed that the field on the adatom where the mesh has the highest density of sharp corners fluctuates with a standard deviation of 1.7%.

#### 4. Discussion

The proposed code is designed to simulate various electronic processes near the surface of a nanostructure with any chemical composition and crystallographic orientation. The code outputs the electric field which affects the interatomic potential in MD and energy barriers in KMC simulations. To calculate those changes, the latter simulations require additional information on surface dipoles [38], while in MD, models similar to the ones suggested in [5], [6] can be used to approximate the charge induced on surface atoms. Furthermore, the high electric field initiates electron emission currents in the material, which may significantly affect the thermal evolution of the system [25], [39], [40] and cause electromigration and must therefore also be taken into account in atomistic simulations.

One important feature of the developed method is its ability to efficiently solve several differential equations of interest on the same mesh. The equations can be solved both in the vacuum and material domain and the solution can easily and efficiently be transferred between those regions. Thus the

method provides a framework for efficiently performing multiphysics calculations that are self-consistently coupled with large-scale atomistic simulations.

Currently we have implemented and verified only the 3D Laplace solver. However, preliminary tests have shown the possibility of also solving 3D heat and continuity equations, which would allow taking the effects of field emission into account more accurately. Moreover, our method provides the framework for analyzing mechanical stress in simulations where this quantity is not inherent but still desired. For instance, the stress due to electric field can be introduced in KMC simulations.

Finally, the current implementation of the code is optimized for geometries that have vertical cylindrical symmetry, like a single nanotip on a substrate, as the mesh will be automatically and efficiently coarsened there. However, the framework of the code also enables adding efficient coarsening schemes for other types of systems like a set of nanotips, ridges or plateaus.

## **5. Conclusions**

We have developed a code to couple atomistic simulations with a finite element solver. Our algorithms dynamically build an unstructured mesh with optimized density that follows the material surface. After calculating the electric field and other physical quantities of interest on the mesh, the code exports the results back to the atomistic simulation. Our method provides the framework for efficiently, concurrently and self-consistently performing multiscale-multiphysics calculations.

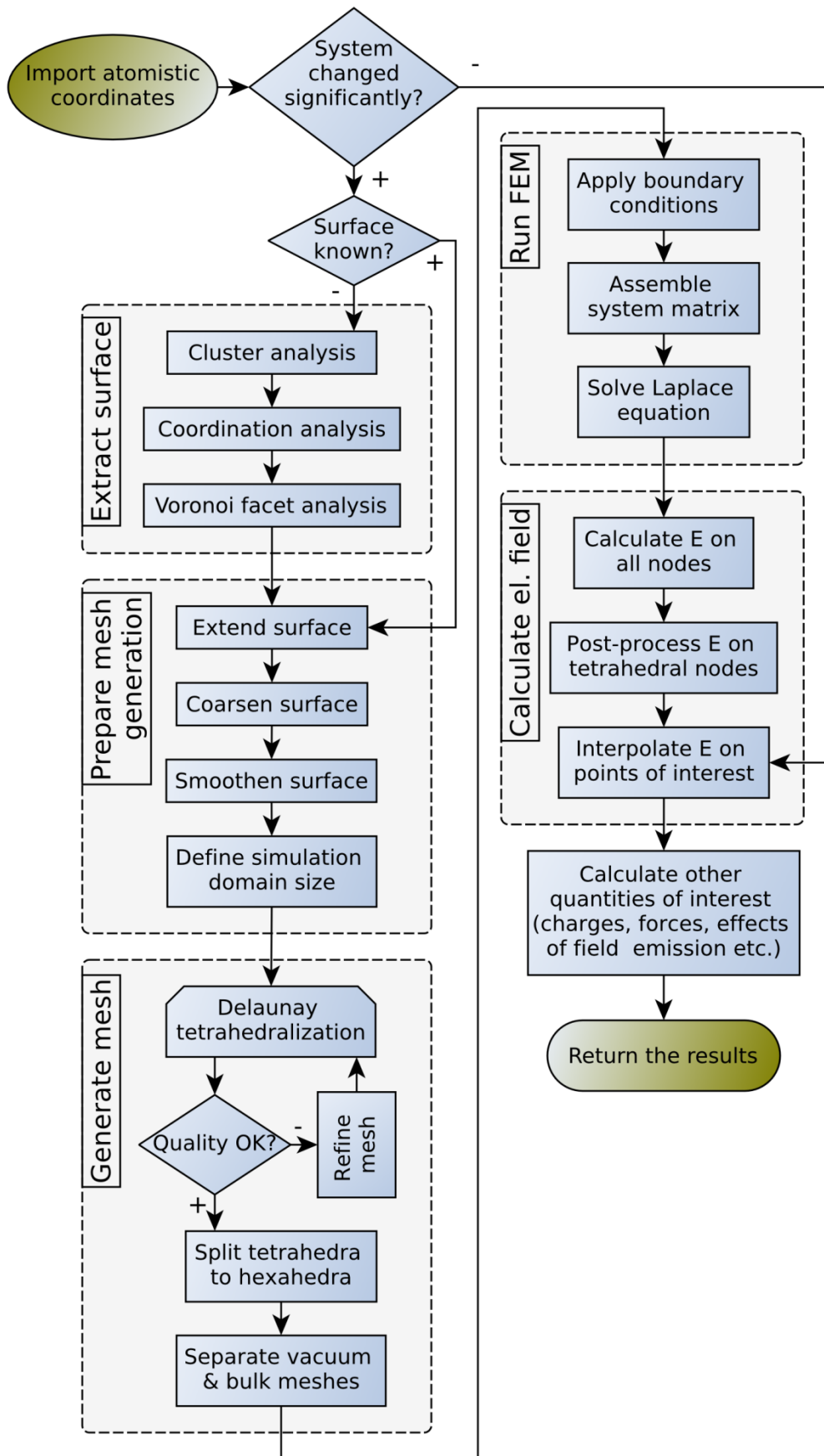
## **Acknowledgements**

The current study was supported by the Academy of Finland project AMELIS, Estonian Research Council Grants PUT 57 and PUT 1372 and the national scholarship program Kristjan Jaak, which is funded and managed by the Archimedes Foundation in collaboration with the Ministry of Education and Research of Estonia. We also acknowledge grants of computer capacity from the Finnish Grid and Cloud Infrastructure (persistent identifier urn:nbn:fi:research-infras-2016072533).

To speed up the development time, the current project takes advantage of several open-source and freely available software packages. The Delaunay tetrahedralization is performed with the C++ library Tetgen [30]. For FEM we use the C++ library Deal.II [31]. Several geometric operations are performed with the aid of C++ library CGAL [34]. The results of the simulations were visualized with the programs OVITO [41] and ParaView [42]. We thank all the people who have contributed to those projects.



## Appendix A. Summary of the code



## Appendix B. Validating the results

The electric potential  $\Phi$  around a hemispherical protrusion residing on the center of the x-y plane can be expressed as [43]

$$\Phi(\mathbf{r}) = -E_0 \cdot z \cdot \left[ 1 - \left( \frac{R}{|\mathbf{r}|} \right)^3 \right], \quad (13)$$

where  $R$  is the radius of the hemisphere and  $E_0$  is the long-range applied electric field. By plugging equation (13) into (4), we obtain the analytical distribution of the electric field:

$$\frac{\mathbf{E}_a(\mathbf{r})}{E_0} = \frac{3R^3 xz}{|\mathbf{r}|^5} \mathbf{i} + \frac{3R^3 yz}{|\mathbf{r}|^5} \mathbf{j} + \left( 1 - R^3 \frac{x^2 + y^2 - 2z^2}{|\mathbf{r}|^5} \right) \mathbf{k}. \quad (14)$$

Denoting the local field near the nanostructure apex ( $x = y = 0, z = R$ ) as  $E_{apex}$ , we define the field enhancement factor as

$$\gamma = \frac{E_{apex}}{E_0}. \quad (15)$$

According to equation (14), the analytical value of  $\gamma$  factor for a hemisphere on a planar surface is

$$\gamma_a = 3. \quad (16)$$

The numerically calculated field values depend on the anode-cathode distance  $d$  and the half-width  $D$  of the substrate (see figure 6). Equation (16) is valid if  $d$  and  $D$  are infinite. In simulations, however, finite  $d$  and  $D$  must be used, thus causing systematic error in the results. We can estimate this systematic error by comparing long-range field values to the ones on the system boundaries, where constraints have been imposed. Doing so, implies

$$\frac{E_a(0,0,d)}{E_a(0,0,\infty)} = 1 + 2 \left( \frac{R}{d} \right)^3, \quad (17)$$

$$\frac{E_a(D,0,0)}{E_a(\infty,0,0)} = \frac{E_a(0,D,0)}{E_a(0,\infty,0)} = 1 - \left( \frac{R}{D} \right)^3. \quad (18)$$

Given the stability of the Laplace equation, the above equations give a rough estimation of how the overall error depends on the system size. Therefore, to keep the estimated systematic error in our simulations below 1%, we always apply the long-range electric field at least 6 times higher than the nanostructure height ( $d \geq 6R$ ) and make the simulation box at least 5 times wider ( $D \geq 5R$ ).

## References

- [1] Y. T. Gu and L. C. Zhang, "A Concurrent Multiscale Method Based on the Meshfree Method and Molecular Dynamics Analysis," *Multiscale Model. Simul.*, vol. 5, no. 4, pp. 1128–1155, 2006.
- [2] V. Iacobellis and K. Behdinin, "Multiscale coupling using a finite element framework at finite temperature," *Int. J. Numer. Methods Eng.*, vol. 92, no. 7, pp. 652–670, 2012.
- [3] L. E. Shilkrot, R. E. Miller, and W. A. Curtin, "Multiscale plasticity modeling: coupled atomistics and discrete dislocation mechanics," *J. Mech. Phys. Solids*, vol. 52, no. 4, pp. 755–787, 2004.
- [4] L. Xiong, G. Tucker, D. L. McDowell, and Y. Chen, "Coarse-grained atomistic simulation of dislocations," *J. Mech. Phys. Solids*, vol. 59, no. 2, pp. 160–177, 2011.
- [5] F. Djurabekova, S. Parviainen, A. Pohjonen, and K. Nordlund, "Atomistic modeling of metal surfaces under electric fields: Direct coupling of electric fields to a molecular dynamics algorithm," *Phys. Rev. E*, vol. 83, no. 2, p. 026704, 2011.
- [6] C. Oberdorfer, S. M. Eich, and G. Schmitz, "A full-scale simulation approach for atom probe tomography," *Ultramicroscopy*, vol. 128, pp. 55–67, 2013.
- [7] J. A. Templeton, R. E. Jones, J. W. Lee, J. A. Zimmerman, and B. M. Wong, "A Long-Range Electric Field Solver for Molecular Dynamics Based on Atomistic-to-Continuum Modeling," *J. Chem. Theory Comput.*, vol. 7, no. 6, pp. 1736–1749, 2011.
- [8] Z. Xu *et al.*, "Simulation of heterogeneous atom probe tip shapes evolution during field evaporation using a level set method and different evaporation models," *Comput. Phys. Commun.*, vol. 189, pp. 106–113, 2015.
- [9] T. Guillet and R. Teyssier, "A simple multigrid scheme for solving the Poisson equation with arbitrary domain boundaries," *J. Comput. Phys.*, vol. 230, no. 12, pp. 4756–4771, 2011.
- [10] C. Z. Antoine, F. Peauger, and F. Le Pimpec, "Electromigration occurrences and its effects on metallic surfaces submitted to high electromagnetic field: A novel approach to breakdown in accelerators," *Nucl. Instrum. Methods Phys. Res. Sect. Accel. Spectrometers Detect. Assoc. Equip.*, vol. 665, pp. 54–69, Feb. 2011.
- [11] H. Yanagisawa *et al.*, "Laser-induced asymmetric faceting and growth of nano-protrusion on a tungsten tip," *APL Photonics*, vol. 1, no. 9, p. 091305.
- [12] F. Vurpillot and C. Oberdorfer, "Modeling Atom Probe Tomography: A review," *Ultramicroscopy*, vol. 159, pp. 202–216, Dec. 2015.
- [13] M. Günther, Ed., *Coupled Multiscale Simulation and Optimization in Nanoelectronics*, vol. 21. Berlin, Heidelberg: Springer Berlin Heidelberg, 2015.
- [14] N. Rozario, H. F. Lenzing, K. F. Reardon, M. S. Zarro, and C. G. Baran, "Investigation of Telstar 4 spacecraft Ku-band and C-band antenna components for multipactor breakdown," *IEEE Trans. Microw. Theory Tech.*, vol. 42, no. 4, pp. 558–564, 1994.
- [15] M. Aicheler and CERN, *A Multi-TeV linear collider based on CLIC technology: CLIC Conceptual Design Report*. Geneva: CERN, 2012.
- [16] P.G. Slade, *Vacuum Interrupter: Theory, Design, and Application*. CRC Press, 2007.
- [17] F. Le Pimpec, R. Ganter, and R. Betemps, "Field emission dark current of technical metallic electrodes," *Nucl. Instrum. Methods Phys. Res. Sect. Accel. Spectrometers Detect. Assoc. Equip.*, vol. 574, no. 1, pp. 7–16, Apr. 2007.
- [18] G. M. McCracken, "A review of the experimental evidence for arcing and sputtering in tokamaks," *Journal of Nuclear Materials*, vol. 93, pp. 3–16, 1980.
- [19] C. Oberdorfer and G. Schmitz, "On the Field Evaporation Behavior of Dielectric Materials in Three-Dimensional Atom Probe: A Numeric Simulation," *Microsc. Microanal.*, vol. 17, no. 01, pp. 15–25, 2011.
- [20] N. Rolland, F. Vurpillot, S. Duguay, and D. Blavette, "A Meshless Algorithm to Model Field Evaporation in Atom Probe Tomography," *Microsc. Microanal.*, vol. 21, no. 06, pp. 1649–1656, 2015.
- [21] M. Veske, S. Parviainen, V. Zadin, A. Aabloo, and F. Djurabekova, "Electrodynamics-molecular dynamics simulations of the stability of Cu nanotips under high electric field," *J. Phys. Appl. Phys.*, vol. 49, no. 21, p. 215301, 2016.

- [22] F. Granberg, S. Parviainen, F. Djurabekova, and K. Nordlund, “Investigation of the thermal stability of Cu nanowires using atomistic simulations,” *J. Appl. Phys.*, vol. 115, no. 21, p. 213518, 2014.
- [23] A. S. Pohjonen, S. Parviainen, T. Muranaka, and F. Djurabekova, “Dislocation nucleation on a near surface void leading to surface protrusion growth under an external electric field,” *J. Appl. Phys.*, vol. 114, no. 3, p. 033519, 2013.
- [24] A. S. Pohjonen, F. Djurabekova, K. Nordlund, A. Kuronen, and S. P. Fitzgerald, “Dislocation nucleation from near surface void under static tensile stress in Cu,” *J. Appl. Phys.*, vol. 110, no. 2, p. 023509, 2011.
- [25] S. Parviainen, F. Djurabekova, H. Timko, and K. Nordlund, “Electronic processes in molecular dynamics simulations of nanoscale metal tips under electric fields,” *Comput. Mater. Sci.*, vol. 50, no. 7, pp. 2075–2079, 2011.
- [26] S. Parviainen, F. Djurabekova, A. Pohjonen, and K. Nordlund, “Molecular dynamics simulations of nanoscale metal tips under electric fields,” *Nucl. Instrum. Methods Phys. Res. Sect. B Beam Interact. Mater. At.*, vol. 269, no. 14, pp. 1748–1751, 2011.
- [27] O. C. Zienkiewicz, R. L. Taylor, and J. Z. Zhu, *The finite element method: its basis and fundamentals*, Seventh edition. Amsterdam: Elsevier, Butterworth-Heinemann, 2013.
- [28] V. Jansson, E. Baibuz, and F. Djurabekova, “Long-term stability of Cu surface nanotips,” *Nanotechnology*, vol. 27, no. 26, p. 265708, 2016.
- [29] M. Ester, H.-P. Kriegel, J. Sander, and X. Xu, “A density-based algorithm for discovering clusters in large spatial databases with noise,” *Kdd*, vol. 96, no. 34, pp. 226–231, 1996.
- [30] H. Si, “TetGen, a Delaunay-Based Quality Tetrahedral Mesh Generator,” *ACM Trans. Math. Softw.*, vol. 41, no. 2, p. 36, 2015.
- [31] W. Bangerth, R. Hartmann, and G. Kanschat, “deal.II — a general-purpose object-oriented finite element library,” *ACM Trans. Math. Softw.*, vol. 33, no. 4, p. 24/1-24/27, 2007.
- [32] I. Amidror, “Scattered data interpolation methods for electronic imaging systems: a survey,” *J. Electron. Imaging*, vol. 11, no. 2, pp. 157–176, 2002.
- [33] J. Vince, “Barycentric Coordinates,” in *Mathematics for Computer Graphics*, 4th ed., Bournemouth, UK: Springer, pp. 203–229.
- [34] C. Delage and O. Devillers, “Spatial Sorting,” in *CGAL User and Reference Manual*, 4.9., CGAL Editorial Board, 2016.
- [35] B. Hegyi and S.-M. Jung, “On the stability of Laplace’s equation,” *Appl. Math. Lett.*, vol. 26, no. 5, pp. 549–552, May 2013.
- [36] “FEMOCS.” [Online]. Available: <https://github.com/veskem/femocs>.
- [37] J. D. Honeycutt and H. C. Andersen, “Molecular dynamics study of melting and freezing of small Lennard-Jones clusters,” *J. Phys. Chem.*, vol. 91, no. 19, pp. 4950–4963, 1987.
- [38] T. T. Tsong and G. Kellogg, “Direct observation of the directional walk of single adatoms and the adatom polarizability,” *Phys. Rev. B*, vol. 12, no. 4, p. 1343, 1975.
- [39] K. Eimre, S. Parviainen, A. Aabloo, F. Djurabekova, and V. Zadin, “Application of the general thermal field model to simulate the behaviour of nanoscale Cu field emitters,” *J. Appl. Phys.*, vol. 118, no. 3, p. 033303, Jul. 2015.
- [40] A. Kyritsakis and F. Djurabekova, “A general computational method for electron emission and thermal effects in field emitting nanotips,” *Comput. Mater. Sci.*, vol. 128, pp. 15–21, 2017.
- [41] A. Stukowski, “Visualization and analysis of atomistic simulation data with OVITO—the Open Visualization Tool,” *Model. Simul. Mater. Sci. Eng.*, vol. 18, no. 1, p. 015012, 2010.
- [42] U. Ayachit, *The ParaView Guide: A Parallel Visualization Application*. Kitware, 2015.
- [43] J. H. Jeans, “The Mathematical Theory of Electricity and Magnetism,” in *The Mathematical Theory of Electricity and Magnetism*, 5th ed., Cambridge: Cambridge University Press, 1927, p. 194.